Satellites detect a methane ultra-emission event from an offshore platform in the Gulf of Mexico

Authors: Itziar Irakulis-Loitxate [1‡*], Javier Gorroño [1‡], Daniel Zavala-Araiza [2,3], Luis Guanter[1,2]

[1] Research Institute of Water and Environmental Engineering (IIAMA), Universitat Politècnica de València (UPV), 46022, Valencia, Spain.

[2] Environmental Defense Fund, Reguliersgracht 79, 1017 LN Amsterdam, The Netherlands.

[3] Institute for Marine and Atmospheric Research Utrecht, Utrecht University, 3584 CC Utrecht, The Netherlands.

‡These authors contributed equally.

* Correspondence to: iiraloi@doctor.upv.es

ABSTRACT

Mitigation of methane emissions from fossil fuel extraction, processing and transport is one of the most effective ways to slow global warming. Satellite-based methods are being instrumental for the detection, characterization, and quantification of this type of emissions. However, despite the rapid development of satellite-based methane plume detection methods for terrestrial surfaces, there is still an important observational gap with respect to offshore oil and gas infrastructure— which accounts for roughly 30% of global production. This is mostly caused by the low reflectivity of water at the shortwave infrared wavelengths used for methane remote sensing. In this work, we have used observations from the WorldView-3 and Landsat 8 satellite missions in a particular observation-illumination geometry to image offshore methane plumes from space. The study site is an offshore oil and gas production platform in the Gulf of Mexico, near the coast of Campeche, in one of Mexico's major oil producing fields. Our data suggest that the platform vented high volumes of methane during a 17-day ultra-emission event, amounting to 0.04 ± 0.01 Tg of methane released to the atmosphere if integrated over time. Our results illustrate how satellites can detect methane plumes from offshore infrastructure, which represents a significant breakthrough in the monitoring of industrial methane emissions from space.

INTRODUCTION

Methane (CH_4) is the second most important anthropogenic greenhouse gas[1]. Significantly reducing CH_4 emissions has been recognized as an essential opportunity in order to reduce the rate of global warming in the short and medium-term[2,3]. However, emitting sectors have significant uncertainty about the amount, location, and duration of emissions[4]. Among them, the emissions derived from the oil and gas (O&G) sector stand out[5,6], since a large fraction of these emissions can be reduced with currently available, highly cost-effective technologies [7].

In order to mitigate these emissions as soon as possible, great efforts are being made to develop more efficient monitoring methods for O&G infrastructure. New methods in CH_4 emissions detection from high- and mid-resolution satellites have successfully demonstrated their effectiveness in numerous studies[8–14]. For example, GHGSat, Sentinel-2 (S2), Landsat, PRISMA, Gaofen5, ZY1-AHSI, and WorldView3 (WV3) satellites measuring backscattered solar radiation in the shortwave infrared (SWIR) spectral region have demonstrated a detection capability of at least ~30-1800 kg CH_4/h for a range of continental O&G extraction regions [9,12,14,15]. However, at the time of this study, none of those satellite systems has been shown to be capable of detecting emissions from offshore O&G operations. This represents a strong limitation in our capability to

monitor industrial CH_4 emissions from space, as offshore O&G production constitutes about 28% of the world's total O&G production[16,17].

The satellite limitations to detect CH_4 over water has led to a lower number of measurement-based, top-down studies, mostly performed from airplanes or ships, resulting in temporally constrained emissions characterization and making it challenging to monitor intermittent emission events [18–22].

The main difficulty for the detection of offshore CH_4 emissions from space is the high absorption of water in the SWIR, which limits the amount of reflected light reaching the sensor and, subsequently, the capability of these sensors to disentangle the absorption of CH_4 in the SWIR from the instrument noise and sea surface roughness. However, this limitation can be overcome by satellites measuring solar radiation specularly-reflected by the water surface in the so-called sun-glint observation mode[23] (see Materials and Methods). For this type of observation, the sensor must point to the forward scattering direction of the Sun-target plane. This can be achieved by pointing the platform accordingly in the case of agile platforms (e.g., the case of WorldView-3, GHGSat, and PRISMA missions), or by using the part of the image lying located opposite to the Sun in the case of sensors without pointing ability but with relatively large field-of-views (e.g., Sentinel-2 and Landsat 8).

In this work, we have explored the ability of satellite-based optical imagers for the detection of CH_4 plumes emitted from offshore O&G infrastructure using sun-glint mode acquisitions. We have used data acquired by the WorldView-3 (WV3) SWIR and Landsat 8 (L8) missions to detect and quantify strong CH_4 plumes from an offshore platform in the Gulf of Mexico. This CH_4 plume detections have been combined with satellite-based data of flaring activity from the same platform for the analysis of the emission source and duration.

MATERIALS AND METHODS

Study area:

The initial objective of the study was to explore the feasibility of offshore CH_4 plume detection with the WV3 satellite system. An area with potentially frequent and strong emissions was needed for this experiment. Based on the recent analysis of offshore emissions by Zavala-Araiza et al.[19], we selected a study site at the Mexican side of the Gulf of Mexico, near the coast of Campeche. This is the Zaap offshore field area, which is responsible for roughly 20% of Mexican oil offshore production[24].

The site with detected emissions is the Zaap-C platform, whose main processes include O&G production through a series of wells, first stage separation, in addition to a power generation unit

used for gas injection. There are two boom-type flares linked to the production and separation units, which were the source of emissions detected in this work.

Satellite datasets:

WV3 is a multispectral satellite with eight bands in the SWIR region and 3.7 m spatial resolution. The very high spatial resolution combined with the high SNR makes it possible to pinpoint the emission source with high precision[14]. The satellite incorporates an agile system that can deliver better than a daily revisit over critical infrastructure and is relatively free to adapt the angular configuration close to the sun-glint. On the other hand, its data are on-demand, so it is only helpful for monitoring potential emitters with a known location. The first WV3-SWIR dataset from our study site that we could use for CH_4 mapping (cloud-free and proper angular configuration) was acquired on December 21.

The detection of a strong emission from one of the platforms inside the imaged area motivated a further analysis of the emissions of that platform using open-access multispectral satellites with global coverage, which have also been shown to have sensitivity to CH_4 [12]. Because of the particular characteristics of the orbit, we could track emissions from the platform using archive data from the L8 between 2013 and January 2022. This was not possible for the S2 platform, as our study site did not fall inside the forward scattering region of the S2 swath (see Figure S2).

Emission detection and quantification:

We have detected the offshore CH_4 emissions using the WV3 and L8 high-resolution satellites. The first step is the derivation of CH_4 concentration enhancement (ΔXCH_4) maps.

In our case, the Mexican Gulf images have a near-optimum angular configuration for L8 OLI instrument (see Section S1, Figure S1), which implies a detection limit sufficient for these extreme emissions[25].

The close spectral signature of the ocean's pixels simplified the ΔXCH_4 retrieval algorithm. In both cases, the applied ΔXCH_4 retrieval method is based on the simple band ratio between a band sensitive to CH_4 and a spectrally close band with no sensitivity (or minimum sensitivity). In WV3, we have used band B8 as the band with the highest sensitivity and B5 as the closest band with the lowest sensitivity, and in L8 OLI bands B7 and B6 in the same order. The bands B5 of WV3 and B6 of L8 contain a residual sensitivity to CH_4 transmittance that is compensated during retrieval (see Section S2 for more information).

Once we obtained the ΔXCH_4 enhancement map, we have performed a plume masking to select CH_4 plume pixels and quantify the emission (see Figure S4). Finally, we have converted the

selected pixels into flux rates (Q) applying the IME method[8]. To do so, we have used 1-h average 10-m wind (U10) data from the NASA GEOS-FP meteorological reanalysis product at 0.25° × 0.3125° resolution[26]. See Section S2 for more information about the CH_4 retrieval methodology.

Verification of CH_4 plume detections:

Taking advantage of the almost simultaneous overpass of S2 and WV3 on the same day with 3 minutes and 51 seconds difference, we have compared both data products to verify different properties of the emission environment. The S2 data provides additional information layers (e.g., RGB and Water Vapor) that support the identification of possible error sources (surface artifacts, water roughness changes, water vapor, or smoke) (see Section S4, Figure S9).

In the case of L8, this verification can be performed from the RGB composition of the same image (see Section S4, Figure S10).

Moreover, we have tested WV3 CH_4 retrieval against simulated products based on CH_4 plumes generated from WRF-LES simulations (see Section S3). These simulations have helped us estimate a WV3 detection limit for that image, i.e., the minimum detectable emission flux at that location under those conditions and with the angular configuration of this particular image, which is close to the sun-glint but not optimal (see Figure S1).

Flaring activity tracking:

We have monitored the emission source flaring activity mainly using the FIRMS web[27] platform's VIIRS data (Suomi NPP and NOAA-20). The VIIRS data provide daily diurnal and nocturnal information at 375 m spatial resolution. This resolution provides errors of several meters in the attribution of flaring source coordinates; however, the offshore platforms are sufficiently scattered in the scene to attribute the flaring signal with large confidence to each one of them.

RESULTS AND DISCUSSION

Using WV3 and L8 multispectral satellite SWIR data, we have detected CH_4 plumes at three different dates from the Zaap-C offshore platform (see Figure 1 and Figure S10).
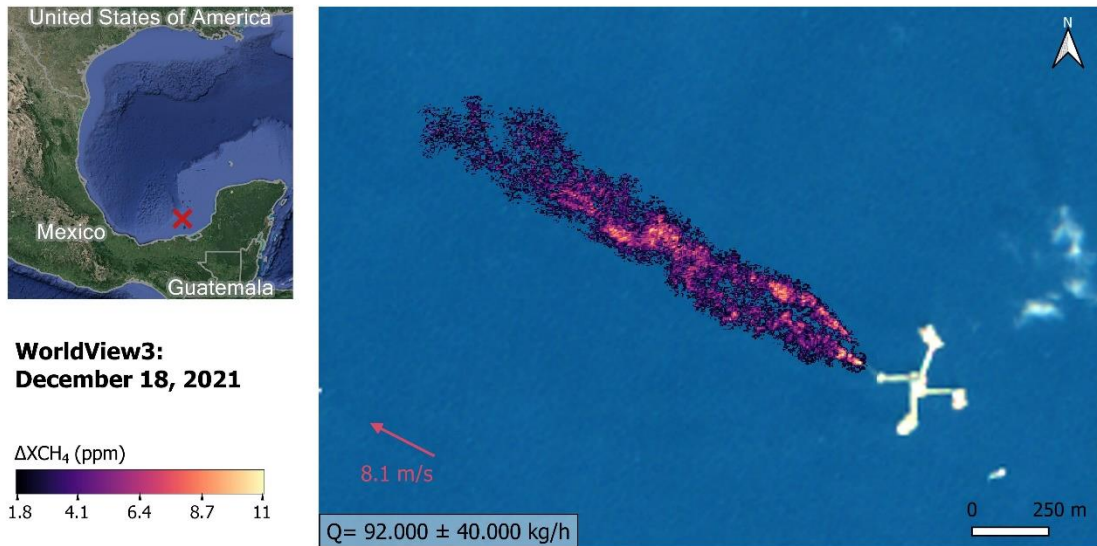
Figure 1. The main panel shows a CH₄ plume from an offshore platform as detected with the WV3 satellite on December 18, 2021. The background image is from a S2 data acquisition from a contiguous non-cloudy day. The map on the left panel indicates the location of the platform in the Gulf of Mexico (source map from Google Earth).

Figure 2 shows the temporal evolution of the flaring at this installation. There, we can appreciate near-constant flare activity over event-previous weeks, when the flare is suddenly turned off from December 8 until December 27, when it is turned back on permanently. In this time range, we can see that on the 16th and 17th, it lights up punctually, as well as on the 17th, 24th, and 26th at night, which indicates short-duration flaring activity intermittency. There is no daily information from S2 and L8, but the analysis of their fire sensitive bands (high emissivity of fire bands B12 and B7, respectively) confirms a flaring stop from day 8 (first day without flaring) to day 28 (first day with flaring after the event).

Therefore, from December 8 to December 27, we have a total of 17 days (excluding days 16 and 17 and the nights of 17, 24, and 26) in which the installation kept the flaring off. The detected three plumes are especially well positioned within this period, covering the event's beginning, middle, and near-end (see Figure 2). Considering that the three plumes have a very similar emission flux (111,000 ± 45,000 kg/h, 92,000 ± 40,000 kg/h, 94,000 ± 38,000 kg/h) we obtain an average emission flux of 99,000 ± 24,000 kg/h assuming no correlation between the estimates. If we consider that the platform was emitting during the whole event with relatively constant flux, as the three detections suggest, we obtain an integrated total emission of 0.04 ± 0.01 Tg of CH₄ in the whole event, calculated as follows:

15 days x 24h + 4 days x 12 h = 408h => 408h * 99,000 kg/h = 40,000,000 ± 10,000,000 kg

An event of this magnitude constitutes 3% of Mexico's annual O&G emissions (1.3 Tg/yr) and this single event would have similar magnitude to the entire regional annual emissions from Mexico's offshore region (0.044 Tg/yr), according to the Shen et al. 2021 study[28].

Although we only show a time series from November 1 to January 27 in Figure 2, the entire VIIRS series (since January 2012) shows very consistent flaring activity at this facility over the years, with few non-cloudy days without flaring data, and the Landsat satellite time series show active flaring since 2008 without a single clear sky day without flaring. Therefore, we deduce that this ultra-emitting event—likely related to abnormal process conditions at the flare—is a one-time incident and with the longest duration since flaring activity began at this platform.
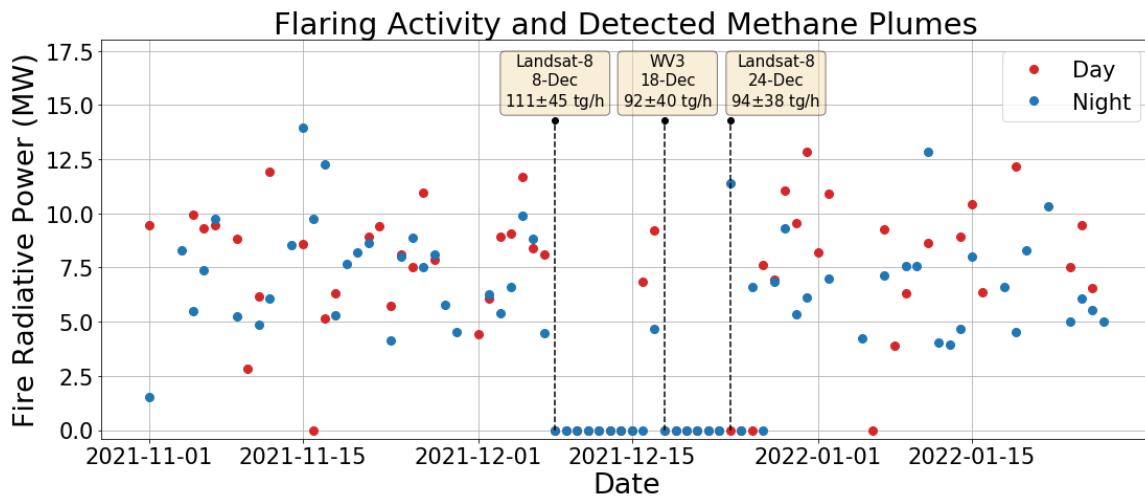

Figure 2. Time series of flaring activity at the offshore platform responsible for the detected methane plumes. Flaring has been plotted as the average value of Fire Radiative Power (in MegaWatts) detected by VIIRS/NOAA-20 and VIIRS/Suomi-NPP. The red dots represent the average value of Fire Radiative Power during the day, and the blue dots the night value. The vertical lines indicate the day when the emissions were detected.

The magnitude of the quantified emission rates through this event differ from those reported in other offshore studies and campaigns [18,19,29], where the highest emissions do not exceed ~3800 kg/h [18]. This may be due to the intermittent nature of flare malfunctions, the relatively small sample size of currently available measurement-based studies, or because the detection methods (airplane, ship, or drone) used in these campaigns sometimes require a pre-warning to the platform operators so that they could anticipate and operate with greater attention the state of the installations. These stochastic events are likely to be unaccounted in current inventories—and if they occur frequently

enough—represent a significant contribution to total emissions for the offshore sector. In the case of Mexican offshore emissions, recent studies[19,28] pointed at a significant overestimation of the national inventory when compared to measurement-based estimates. Nonetheless, if additional events as the one detected in this work happen at other offshore platforms, the discrepancy in the estimates reported in the previous studies with respect to the official inventories could be compensated.

Our work demonstrates the importance of having robust methods that transparently monitor these events. Further work is needed to understand better the prevalence of such events and what fraction of emissions, relative to the total, they represent.

In absence of stringent, measurement-based reporting frameworks, events like this one could easily go unnoticed. The high-resolution acquisitions from these two satellites have proven to be sufficient to attribute the emission to a specific source accurately, even if the plume is located over water. In the case of WV3, its 3.7 m/pix resolution makes it possible to distinguish two plumes emanating from the same installation, which then converge into a single plume downwind. These two sources are probably associated to the two flares at different sections of the platform (i.e., drilling and separation). In the case of L8 OLI, the 30 m resolution is sufficient to detect the origin of the emission and a defined plume. Although the L8 overpass at this offshore platform provides optimum viewing angular conditions (see Figure S1 and Figure S10), the occurrence of the emission during the winter means that the sun zenith angle is substantially high. A better angular configuration would occur closer to the summer solstice, which is expected to reduce the detection limit substantially.

Finally, from the WV3 image simulations, we have estimated that the detection limit of this satellite is around 1500 kg/h for this scene (see Section S3). However, the detection limit over oceans mainly depends on the angular configuration of the acquisition. Even though this acquisition is close to the sun-glint angular configuration, there is certainly room for improvement. That is, a trade-off between target revisit and detection limit is possible to establish in order to define a specific acquisition strategy. Moreover, it is also expected that the detection limit can be further reduced over this same region for other periods of the year. Since the O&G emitters usually follow a long tail distribution (a few sources emit most of the emissions), both onshore and offshore, a lower detection limit would allow identifying most of the emitters detected in previous occasions in the Mexican Gulf of Mexico [19], or disproportionately high emission events that are quite frequent in the U.S. Gulf of Mexico [18]. On the other hand, it should be noted that other factors could strongly affect the detection capability of satellites. The most prominent are the wind speed (the higher the wind speed, the higher the detection limit), which is mostly high at sea, and the roughness of the

sea due to waves (the higher the roughness/waves, the more difficult it will be to detect emissions) [29,30]. Due to these last two characteristics, it is expected that the methods used here to detect offshore emissions in the ocean will obtain even better results in lakes (ideal case) and seas with very calm waters, where waves and wind are much lower.

Our results show that offshore CH_4 monitoring efforts can be improved if they are combined with flaring activity data, as a break in flaring activity can indicate a possible malfunction event. Similarly, it would be helpful the combination with ESA's TROPOMI sensor's low spatial resolution data, which, since November 2021, provides data on the sun-glint areas of the oceans[31]. Unfortunately, the Gulf of Mexico is outside the sun-glint area during the study period, so we could not get complementary information from TROPOMI.

The plumes presented in this work demonstrate that the detection of CH_4 emissions in the ocean is already possible from space, and that we can even monitor them over time as long as scenes are acquired with an adequate angular configuration. The list of satellites with ability for offshore CH_4 mapping can be extended by the PRISMA hyperspectral system and the upcoming EnMAP, MethaneSAT and Carbon Mapper missions, whose spectral configuration and pointing ability meet the requirements for detecting CH_4 over water. These findings represent a new breakthrough in the quickly developing field of high resolution CH_4 mapping from space.

ACKNOWLEDGMENT

REFERENCES

(1)   Etminan, M.; Myhre, G.; Highwood, E. J.; Shine, K. P. Radiative Forcing of Carbon Dioxide, Methane, and Nitrous Oxide: A Significant Revision of the Methane Radiative Forcing. *Geophys. Res. Lett.* **2016**. https://doi.org/10.1002/2016GL071930.

(2)   Control Methane to Slow Global Warming — Fast. *Nature* **2021**, *596* (7873), 461. https://doi.org/10.1038/D41586-021-02287-Y.

(3)   United Nations Environment Programme and Climate and Clean Air Coalition. *Global*

Methane Assessment: Benefits and Costs of Mitigating Methane Emissions; Nairobi: United Nations Environment Programme, 2021.

(4)   Saunois, M.; R. Stavert, A.; Poulter, B.; Bousquet, P.; G. Canadell, J.; B. Jackson, R.; A. Raymond, P.; J. Dlugokencky, E.; Houweling, S.; K. Patra, P.; Ciais, P.; K. Arora, V.; Bastviken, D.; Bergamaschi, P.; R. Blake, D.; Brailsford, G.; Bruhwiler, L.; M. Carlson, K.; Carrol, M.; Castaldi, S.; Chandra, N.; Crevoisier, C.; M. Crill, P.; Covey, K.; L. Curry, C.; Etiope, G.; Frankenberg, C.; Gedney, N.; I. Hegglin, M.; Höglund-Isaksson, L.; Hugelius, G.; Ishizawa, M.; Ito, A.; Janssens-Maenhout, G.; M. Jensen, K.; Joos, F.; Kleinen, T.; B. Krummel, P.; L. Langenfelds, R.; G. Laruelle, G.; Liu, L.; MacHida, T.; Maksyutov, S.; C. McDonald, K.; McNorton, J.; A. Miller, P.; R. Melton, J.; Morino, I.; Müller, J.; Murguia-Flores, F.; Naik, V.; Niwa, Y.; Noce, S.; O'Doherty, S.; J. Parker, R.; Peng, C.; Peng, S.; P. Peters, G.; Prigent, C.; Prinn, R.; Ramonet, M.; Regnier, P.; J. Riley, W.; A. Rosentreter, J.; Segers, A.; J. Simpson, I.; Shi, H.; J. Smith, S.; Paul Steele, L.; F. Thornton, B.; Tian, H.; Tohjima, Y.; N. Tubiello, F.; Tsuruta, A.; Viovy, N.; Voulgarakis, A.; S. Weber, T.; Van Weele, M.; R. Van Der Werf, G.; F. Weiss, R.; Worthy, D.; Wunch, D.; Yin, Y.; Yoshida, Y.; Zhang, W.; Zhang, Z.; Zhao, Y.; Zheng, B.; Zhu, Q.; Zhu, Q.; Zhuang, Q. The Global Methane Budget 2000-2017. *Earth Syst. Sci. Data* **2020**. https://doi.org/10.5194/essd-12-1561-2020.

(5)   (UNEP), U. N. E. P. Oil and Gas Methane Partnership (OGMP) 2.0 Framework | Climate & Clean Air Coalition. 2020, pp 1–18.

(6)   Lauvaux, T.; Giron, C.; Mazzolini, M.; d'Aspremont, A.; Duren, R.; Cusworth, D.; Shindell, D.; Ciais, P. Global Assessment of Oil and Gas Methane Ultra-Emitters. *Science (80-.).* **2021**. https://doi.org/10.1126/SCIENCE.ABJ4351/SUPPL_FILE/SCIENCE.ABJ4351_SM.PDF.

(7)   Ocko, I. B.; Sun, T.; Shindell, D.; Oppenheimer, M.; Hristov, A. N.; Pacala, S. W.; Mauzerall, D. L.; Xu, Y.; Hamburg, S. P. Acting Rapidly to Deploy Readily Available Methane Mitigation Measures by Sector Can Immediately Slow Global Warming. *Environ. Res. Lett.* **2021**, *16* (5), 054042. https://doi.org/10.1088/1748-9326/ABF9C8.

(8)   Varon, D. J.; Jacob, D. J.; Mckeever, J.; Jervis, D.; Durak, B. O. A.; Xia, Y.; Huang, Y. Quantifying Methane Point Sources from Fine-Scale Satellite Observations of Atmospheric Methane Plumes. *Atmos. Meas. Tech* **2018**, *11*, 5673–5686. https://doi.org/10.5194/amt-11-5673-2018.

(9)   Irakulis-Loitxate, I.; Guanter, L.; Liu, Y.-N.; Varon, D. J.; Maasakkers, J. D.; Zhang, Y.; Chulakadabba, A.; Wofsy, S. C.; Thorpe, A. K.; Duren, R. M.; Frankenberg, C.; Lyon, D.

R.; Hmiel, B.; Cusworth, D. H.; Zhang, Y.; Segl, K.; Gorroño, J.; Sánchez-García, E.; Sulprizio, M. P.; Cao, K.; Zhu, H.; Liang, J.; Li, X.; Aben, I.; Jacob, D. J. Satellite-Based Survey of Extreme Methane Emissions in the Permian Basin. *Sci. Adv.* **2021**, *7* (27), eabf4507. https://doi.org/10.1126/SCIADV.ABF4507.

(10)   Varon, D. J.; Jervis, D.; McKeever, J.; Spence, I.; Gains, D.; Jacob, D. J. High-Frequency Monitoring of Anomalous Methane Point Sources with Multispectral Sentinel-2 Satellite Observations. *Atmos. Meas. Tech.* **2021**, *14* (4), 2771–2785. https://doi.org/10.5194/amt-14-2771-2021.

(11)   Guanter, L.; Irakulis-Loitxate, I.; Gorroño, J.; Sánchez-garcía, E.; Cusworth, D. H.; Varon, D. J.; Cogliati, S.; Colombo, R. Mapping Methane Point Emissions with the PRISMA Spaceborne Imaging Spectrometer (Under Review). *Remote Sens. Environ.* **2021**.

(12)   Irakulis-Loitxate, I.; Guanter, L.; Maasakkers, J. D.; Zavala-Araiza, D.; Aben, I. Satellites Detect Abatable Super-Emissions in One of the World's Largest Methane Hotspot Regions. *Environ. Sci. Technol.* **2022**, acs.est.1c04873. https://doi.org/10.1021/ACS.EST.1C04873.

(13)   Cusworth, D. H.; Duren, R. M.; Thorpe, A. K.; Pandey, S.; Maasakkers, J. D.; Aben, I.; Jervis, D.; Varon, D. J.; Jacob, D. J.; Randles, C. A.; Gautam, R.; Omara, M.; Schade, G. W.; Dennison, P. E.; Frankenberg, C.; Gordon, D.; Lopinto, E.; Miller, C. E. Multisatellite Imaging of a Gas Well Blowout Enables Quantification of Total Methane Emissions. *Geophysical Research Letters*. 2021. https://doi.org/10.1029/2020GL090864.

(14)   Sánchez-García, E.; Gorroño, J.; Irakulis-Loitxate, I.; Varon, D.; Guanter, L. Mapping Methane Plumes at Very High Spatial Resolution with the WorldView-3 Satellite. *Atmos. Meas. Tech. Discuss.* **2021**, 1–26. https://doi.org/10.5194/AMT-2021-238.

(15)   Varon, D.; Jervis, D.; McKeever, J.; Spence, I.; Gains, D.; Jacob, D. High-Frequency Monitoring of Anomalous Methane Point Sources with Multispectral Sentinel-2 Satellite Observations. *Atmos. Meas. Tech. Discuss.* **2020**, No. December, 1–21. https://doi.org/10.5194/amt-2020-477.

(16)   Global crude oil onshore and offshore production distribution 2025 | Statista https://www.statista.com/statistics/624138/distribution-of-crude-oil-production-worldwide-onshore-and-offshore/ (accessed Jan 27, 2022).

(17)   Rystad Energy - Your Energy Knowledge House https://www.rystadenergy.com/ (accessed Apr 18, 2021).

(18)   Gorchov Negron, A. M.; Kort, E. A.; Conley, S. A.; Smith, M. L. Airborne Assessment of Methane Emissions from Offshore Platforms in the U.S. Gulf of Mexico. *Environ. Sci.*

Technol. **2020**, *54* (8), 5112–5120.
https://doi.org/10.1021/ACS.EST.0C00179/SUPPL_FILE/ES0C00179_SI_001.PDF.

(19) Zavala-Araiza, D.; Omara, M.; Gautam, R.; Smith, M. L.; Pandey, S.; Aben, I.; Almanza-Veloz, V.; Conley, S.; Houweling, S.; Kort, E. A.; Maasakkers, J. D.; Molina, L. T.; Pusuluri, A.; Scarpelli, T.; Schwietzke, S.; Shen, L.; Zavala, M.; Hamburg, S. P. A Tale of Two Regions: Methane Emissions from Oil and Gas Production in Offshore/Onshore Mexico A Tale of Two Regions: Methane Emissions from Oil and Gas Production in Offshore/Onshore Mexico. *Environ. Res. Lett* **2021**, *16*, 24019. https://doi.org/10.1088/1748-9326/abceeb.

(20) Yacovitch, T. I.; Daube, C.; Herndon, S. C. Methane Emissions from Offshore Oil and Gas Platforms in the Gulf of Mexico. *Environ. Sci. Technol.* **2020**, *54* (6), 3530–3538. https://doi.org/10.1021/ACS.EST.9B07148.

(21) Foulds, A.; Allen, G.; Shaw, J. T.; Bateson, P.; Barker, P. A.; Huang, L.; Pitt, J. R.; Lee, J. D.; Wilde, S. E.; Dominutti, P.; Purvis, R. M.; Lowry, D.; France, J. L.; Fisher, R. E.; Fiehn, A.; Pühl, M.; B Bauguitte, S. J.; Conley, A.; Smith, M. L.; Lachlan-Cope, T.; Pisso, I.; Schwietzke, S. Quantification and Assessment of Methane Emissions from Offshore Oil and Gas Facilities on the Norwegian Continental Shelf. *Atmos. Chem. Phys.* https://doi.org/10.5194/acp-2021-872.

(22) France, J. L.; Bateson, P.; Dominutti, P.; Allen, G.; Andrews, S.; Bauguitte, S.; Coleman, M.; Lachlan-Cope, T.; Fisher, R. E.; Huang, L.; Jones, A. E.; Lee, J.; Lowry, D.; Pitt, J.; Purvis, R.; Pyle, J.; Shaw, J.; Warwick, N.; Weiss, A.; Wilde, S.; Witherstone, J.; Young, S. Facility Level Measurement of Offshore Oil and Gas Installations from a Medium-Sized Airborne Platform: Method Development for Quantification and Source Identification of Methane Emissions. *Atmos. Meas. Tech.* **2021**, *14* (1), 71–88. https://doi.org/10.5194/AMT-14-71-2021.

(23) Larsen, N. F.; Stamnes, K. H. Methane Detection from Space: Use of Sunglint. *Opt. Eng.* **2006**, *45* (1), 016202. https://doi.org/10.1117/1.2150835.

(24) CNIH - Sistema de Información de Hidrocarburos (SIH) https://sih.hidrocarburos.gob.mx/ (accessed Mar 23, 2022).

(25) Gatebe, C. K.; Wilcox, E.; Poudyal, R.; Wang, J. Effects of Ship Wakes on Ocean Brightness and Radiative Forcing over Ocean. *Geophys. Res. Lett.* **2011**, *38* (17). https://doi.org/10.1029/2011GL048819.

(26) Molod, A.; Takacs, L.; Suarez, M.; Bacmeister, J.; Song, I.-S.; Eichmann, A. The GEOS-5 Atmospheric General Circulation Model: Mean Climate and Development from MERRA

to Fortuna. *NASA TM-2012-104606* **2012**.

(27) NASA | LANCE | FIRMS https://firms.modaps.eosdis.nasa.gov/ (accessed Jul 12, 2021).

(28) Shen, L.; Zavala-Araiza, D.; Gautam, R.; Omara, M.; Scarpelli, T.; Sheng, J.; Sulprizio, M. P.; Zhuang, J.; Zhang, Y.; Qu, Z.; Lu, X.; Hamburg, S. P.; Jacob, D. J. Unravelling a Large Methane Emission Discrepancy in Mexico Using Satellite Observations. *Remote Sens. Environ.* **2021**, *260*, 112461. https://doi.org/10.1016/J.RSE.2021.112461.

(29) Brown, P. F.; Saunier, S.; Simon, M.; Heras Cruz, B. *Overview of Methane Detection and Measurement Technologies for Offshore Applications* ; 2020.

(30) Gatebe, C. K.; King, M. D. Airborne Spectral BRDF of Various Surface Types (Ocean, Vegetation, Snow, Desert, Wetlands, Cloud Decks, Smoke Layers) for Remote Sensing Applications. *Remote Sens. Environ.* **2016**, *179*, 131–148. https://doi.org/10.1016/J.RSE.2016.03.029.

(31) Landgraf, J.; Lorente, A.; Langerock, B.; Kumar Sha BIRA-, M. S5P Mission Performance Centre Methane [L2__CH4___] Readme Document Number Issue 2.1 Date Status Prepared By. **2021**.

Supplementary Information for

Satellites detect a methane ultra-emission event from an offshore platform in the Gulf of Mexico.

Authors: Itziar Irakulis-Loitxate [1‡*], Javier Gorroño [1‡], Daniel Zavala-Araiza [2,3], Luis Guanter[1,2]

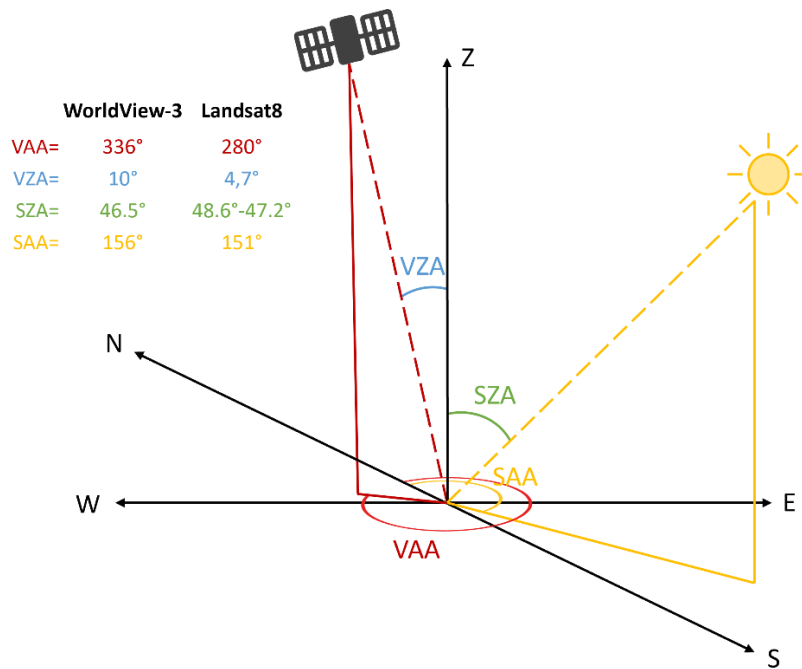* Correspondence to: iiraloi@doctor.upv.es

This section includes:

Section 1. Image configuration

Figure S1: WV3 and L8 scenes angular configuration. Both satellite scene acquisitions are in the forward scatter plane with WV3 acquisition near sun glint angular configuration. In the image, we represent their relative position with the sun. Each angle parameter is indicated on the left side alongside its value (VAA refers to viewing azimuth angle, VZA refers to viewing zenith angle, SZA refers to sun zenith angle and SAA refers to sun azimuth angle). The angles in the image are just indicative.
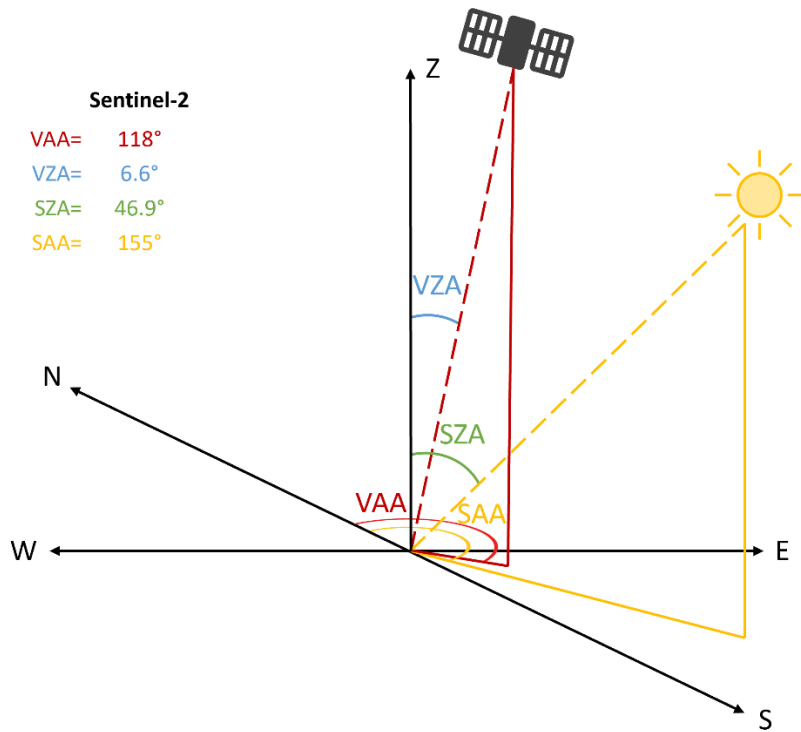
Figure S2: S2 scene angular configuration. The S2 near-polar sun synchronous orbit defines a single overpass over this offshore platform (there is no overlapping of another overpass with a different angle), and it is on the backscatter plane (see relative position of SAA and VAA in the image). We indicate the S2 angular parameters of December 18, 2021, as a representative day during the event. The angles in the image are just indicative.

Section 2. Retrieval methodology

The retrieval methodology is based on the one described in Sánchez-García, 2022. This methodology estimates a methane concentration map from pixel-wise estimates of methane transmittance at WV-3 SWIR band 7 (2235–2285 nm). This transmittance is defined by the ratio between this methane-sensitive band against an equivalent band with no excess methane present.

The examples illustrated in Sánchez-García, 2022 (O&G sites in Turkmenistan and Algeria and the coal mines in China) selected a multilinear regression with bands B1-B4 and B6 to estimate B7 with no excess methane. This was a good compromise between an improved retrieval noise and outlier reduction at the cost of a small underestimation of the methane enhancement.
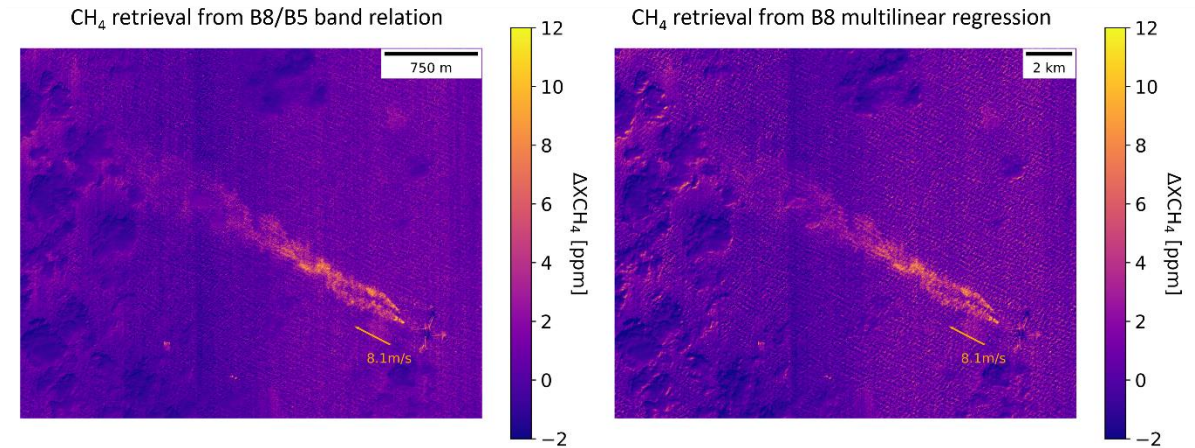
Figure S3: WV3 CH4 retrieval using different methods. In the left CH4 retrieval using B8/B5 band ratio. In le right CH4 retrieval using multilinear regression as was presented by Sánchez-García et al.

The retrieval in this study is performed over an ocean scene rather than a land site. In this scenario, the selection of a multilinear regression does not offer significant improvements over an area with a highly similar spectral signature at a pixel level. The information from more bands does not significantly improve the estimation and reduces the corregistration between the bands. Thus, in this case, the simple ratio between a methane-sensitive band (B7 and B8) and a spectrally closer band defines the methane plume transmittance (B5) (see Figure S3). The latter does contain a residual sensitivity to methane transmittance that is compensated during the retrieval.

Masking takes twice the standard deviation of XCH4 in an area not affected by the methane plume. Here, the selected area is located slightly to the Northeast of the O&G platform with an area of 1100x 1480m. Manually removes the O&G platform shadow and a small cloud shadow next to the origin of the source. Then, a feature recognition algorithm detects the masked areas with a number of pixels larger than a certain threshold of 1250 pixels. Finally, a dilation mask (5-pixel-diameter shape) is applied to the resulting mask to include neighboring pixels (see Figure S4).
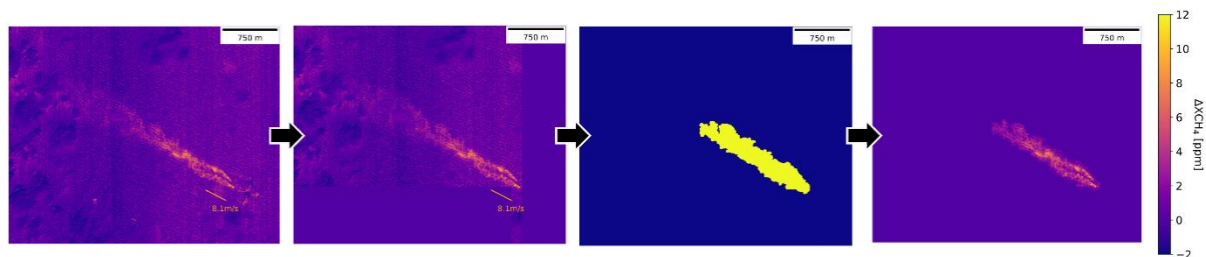

Figure S4: WV3 plume's masking process.

The selected pixels are converted into flux rates applying the IME method.

WV3 emission quantification method

The retrieval noise using B8 was considerably lower than B7 (B8 std 896 ppb against B7 1565 ppb). Both images have a considerable effect of stripping and non-uniformity effects in the across-track direction, which are the consequence of radiometric and spectral variations in the detector (see Figure S5). This constitutes a challenging artifact in ocean scenes where their relative impact is important.
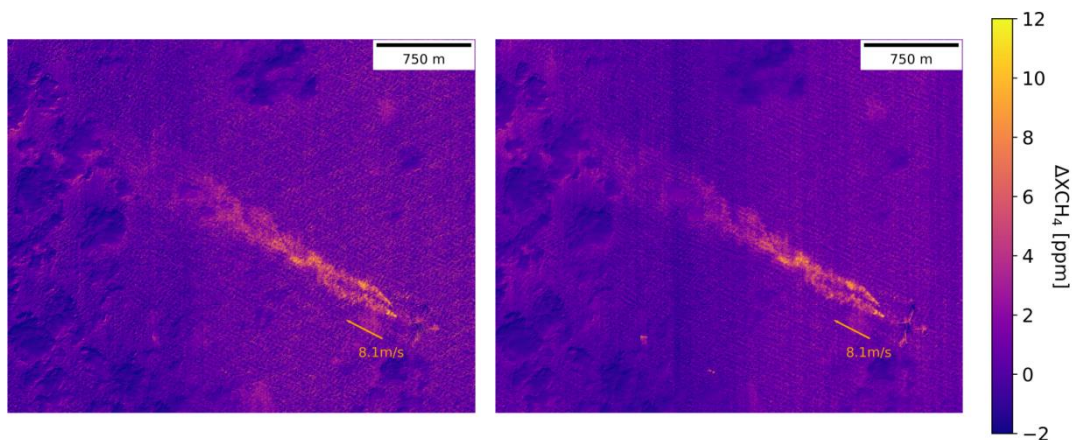

Figure S5: Methane enhancement map for (left) B7/B5 and (right) B8/B5. The wind speed and direction are included in each panel. In both cases, the enhancement map depicts an important emission coming from the O&G platform and closely following the wind direction. In a qualitative approach, this can be considered a massive emission due to the combined high methane enhancement values and wind speed (8.1 m/s).

The mean enhancement in the across-track direction of 200 and 100 rows of the North and South areas of the image suggests a bias of up to 1ppm. Based on the positioning of the plume and the estimated bias, we estimate a bias of ~0.5ppm. This represents a relative bias of 19% on the estimated IME and flux rate that has been included in the final estimates as a correction factor.

Based on the methodology described here with a B8/B5 ratio, the estimated flux is 91853.6 ± 39499 kg/h, IME = 5219.59 kg, and L= 655.255m.

L8 emissions quantification method

To obtain the retrieval of CH4 with L8, the normalized band ratio between B7 and B6 has been applied. Then, we applied the masking similarly to the WV3 process. Quantification has been carried out by the IME method using the model trained for S2 products and adapted to L8 spatial resolution [10]. Since this model has been trained with simulations under closer to terrestrial

conditions, it must be noted that the calculated emission flux estimation has a higher uncertainty than those obtained in onshore emissions.
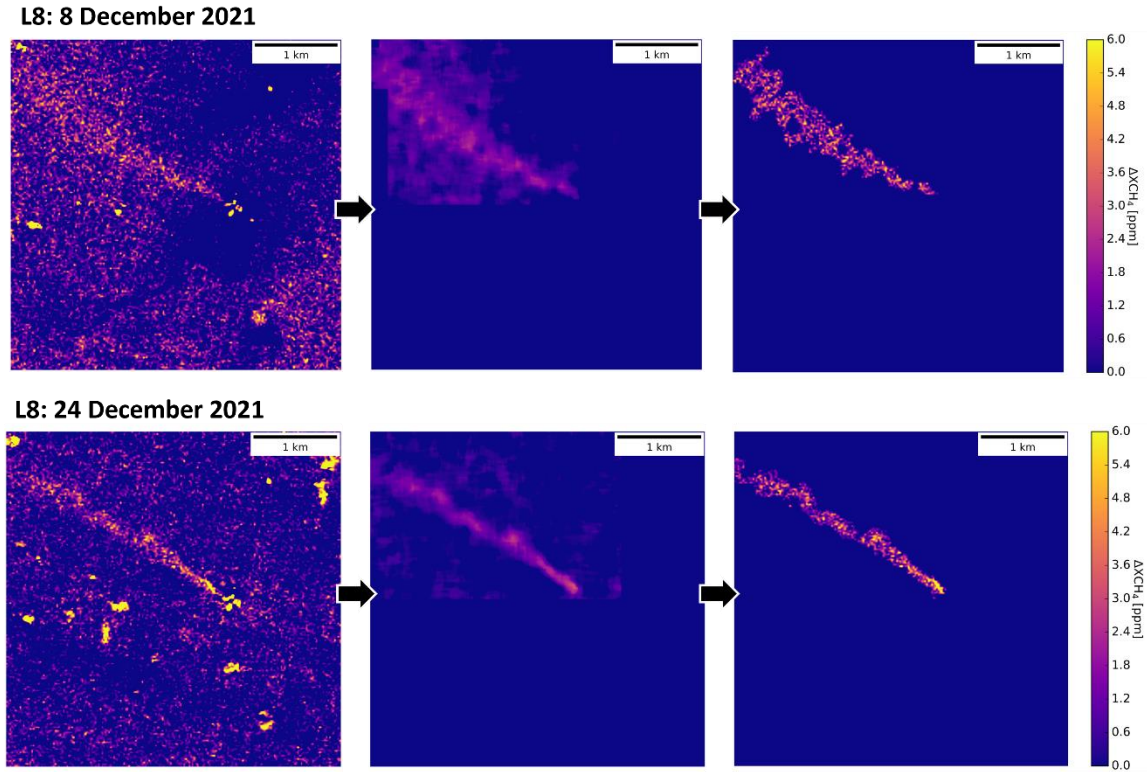
L8: 8 December 2021

L8: 24 December 2021

Figure S6: L8 plumes masking and quantification process.

Based on the methodology described here with a B7/B6 ratio, the estimated flux is 111.000 ± 45.000 kg/h on December 8 and 94.000 ± 38.000 kg/h on December 24.

Section S3. Validation

The validation of WV3 has been performed by selecting a 1.5x1.5km area in the North-East of Figure S5, similar to the area selected for noise calculation.

A range of WV3 simulated products, including methane plumes has been generated. These plumes cover a range of flux rates from 0 to 60t/hr. This is nearly 7000 kg in IME range that are close to the value obtained in the offshore platform retrieval. The validation against the IME reference is shown below:
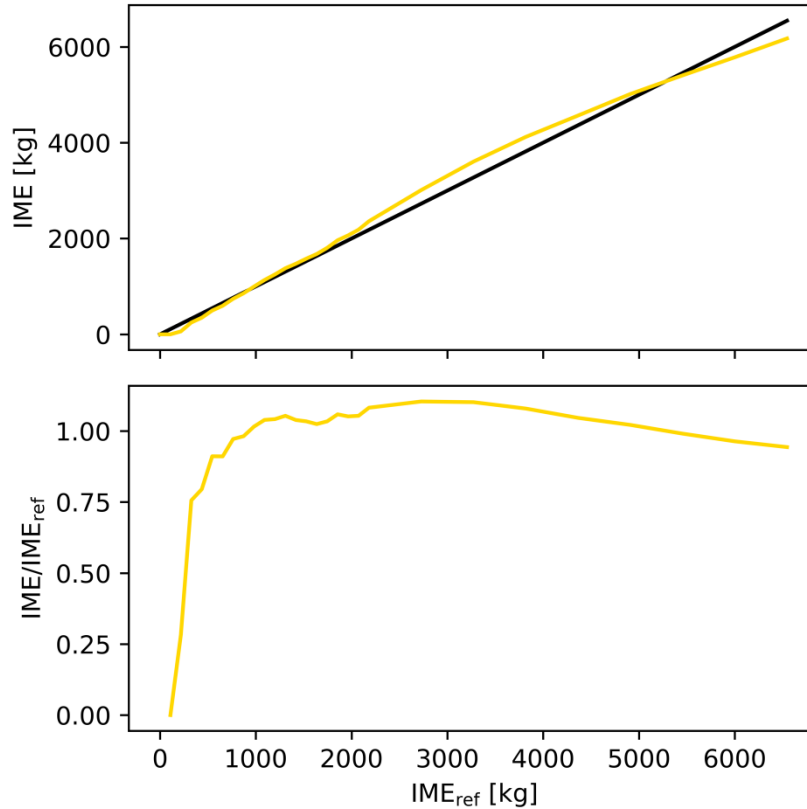
Figure S7: Regression between IME retrieved from WV3 simulated products against reference values. The reference methane plumes cover a range of flux rates from 0 to 60t/hr and the simulated products cover a 1.5x1.5km area in the North-East of Figure S5.

The illustration shows how the retrieval captures part of the plume at a small flux rate levels and the retrieval noise becomes almost negligible at an IME of 1000kg (this approximately represents a Q=10000kg/h) when the retrieval captures almost the entire plume. The IME is slighly overestimated from 1000kg with a slight decline from 4000kg onwards. This occurs due to the saturation of pixels with a very high pixel concentration $\Delta XCH4 > 10ppm$ as a result of an extrapolation of the LUT values during the retrieval process. This well-known effect has a minor effect in the offshore platform retrieval since just a few pixels in the enhancement map are marginally over these levels.

The validation of the flux rate levels is a more challenging process. The original Ueff model for the WV3 mission was originally trained for simulated plumes with plume length L lower than 200m. In the absence of a training dataset with long plumes (L>200), the Ueff model tuned for the PRISMA mission was applied in Sánchez-García, 2022[14]. Both of these models have been tested

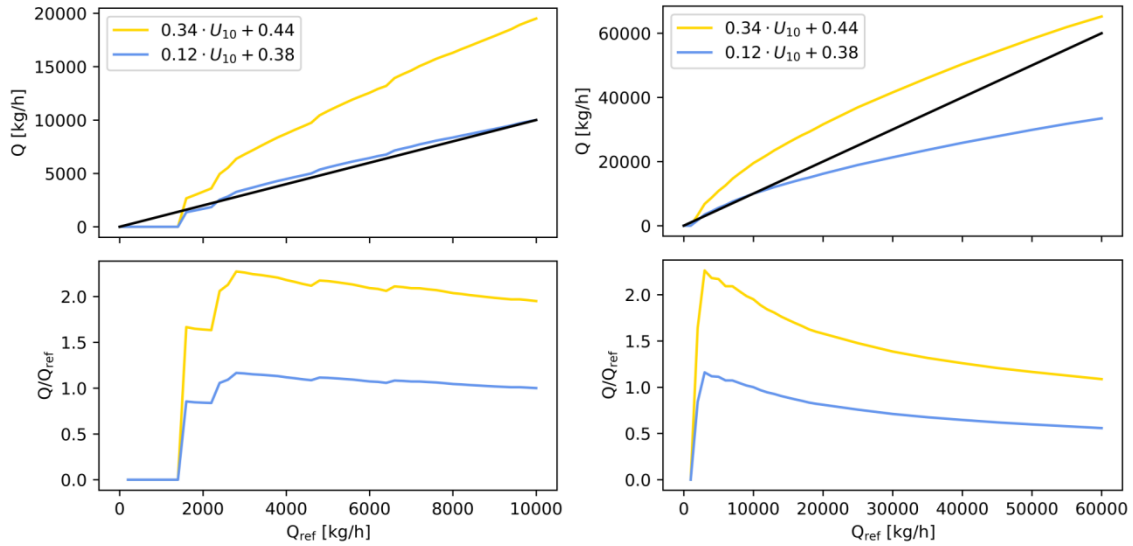for the flux rates up to 60t/hr. The range up to 10t/hr and 60t/hr are presented below in separate figures:

Figure S8: Regression between methane flux rate retrieved from WV3 simulated products against reference values. The reference methane plumes cover a range of flux rates from 0 to 10t/hr (left image) and 0 to 60t/hr (right image). The simulated products cover a 1.5x1.5km area in the North-East of Figure S5.

The results show a very good agreement of the Ueff model tuned for WV3 acquisitons (in blue) up to 10000kg/h. That range covers a plume length that spans from 100 to 300m. From that point onwards, the model systematically underestimates the flux rate. At that point, the results suggest that the Ueff model tuned for PRISMA acquisitions provides a better estimation of the flux rate. For the largest flux rates here shown, the Ueff based on PRISMA produces a slight overestimation (~10%) whereas the Ueff based on WV3 acquisitions indicates a large underestimation (~50%).

Another interesting outcome of this validation exercise is the low plume detection threshold for WV3 over this ocean acquisition. The simulation suggests a theshold below the 2000kg/h which is also coherent comparing with the noise levels reported in Sánchez-García, 2022 (the retrieval noise reported in the offshore platform is ~900ppm). The angular configuration set for this acquisition was at a relative azimuth angle of 180 degrees but a difference of 30 degrees between the viewing and sun zenith angle. This detection threshold is highly dependent on the angular configuration and, based on this analysis, it can be further reduced if the satellite acquisition is closer to the sun-glint angular configuration or slightly increased if the angular conditions are relaxed.

Section S4. False positive absence verification

The WV3 product processed in this study only contains information from the SWIR region (8 bands between 1195 and 2365 nm), making it difficult to completely view the area and the site context. In the absence of information from other spectrum regions, it is also challenging to be fully certain that the observed CH4 enhancement is not coming from other possible false-positive sources. In the case of the plume detected from the WV3 product, the enhancement is clear from a rapid visual inspection. Nonetheless, we have used the near-simultaneous detection of S2 with a difference of 3 minutes and 51 seconds (WV3: 16:52:03 UTC, S2: 16:48:12 UTC) with respect to WV3 to contrast the information from both images and obtain a fuller picture.

The S2 L1C product provides information on the visible spectrum (RGB) or water vapor derived from the B9/B8A band ratio. We show this information in Figure S9, where the emitting platform is marked with a red arrow. In the left window (RGB composite), we see two installations with "white smoke" plumes on the right side of the image. These plumes are water vapor columns that are injected to improve the combustion efficiency of the flares. The water vapor can be seen in the right window, where the vapor plumes are dark black in the two infrastructures on the right, while (despite the proximity of the clouds) this same enhancement is not seen emanating from our emitting infrastructure. This verifies that the detected CH4 plume has nothing to do with water vapor nor with any other artifact that may have been on the scene that day. At the same time, we could see that in the CH4 retrieval, the only clear plume is from the emitting platform, while the other platforms no longer show anything plume-like.
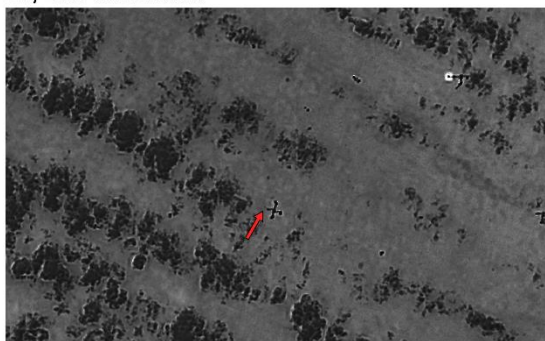

Figure S9: S2 image information minutes before WV3 detection. On the left, visual imagery of the area where we detected the CH4 plume, and on the right is the B9/B8A band ratio that enhances the water vapor. The platform is marked with the red arrow.

In L8, we can verify the absence of false positives due to the water vapor plume or changes in sea surface roughness using the rest of the bands in the same L8 images. In Figure S10, we see how other platforms emit water vapor but the only clear plumes in the retrieval are those of methane, in which we see that there is no water vapor in the RGB images. On day 8, we can see in the retrieval image a plume-like figure created by the denser clouds inside the water vapor plume emanating from the platform on the left. However, we can see that these enhancements are created by the dense clouds, while the real plume has no artifacts that could falsely create the signal enhancement.
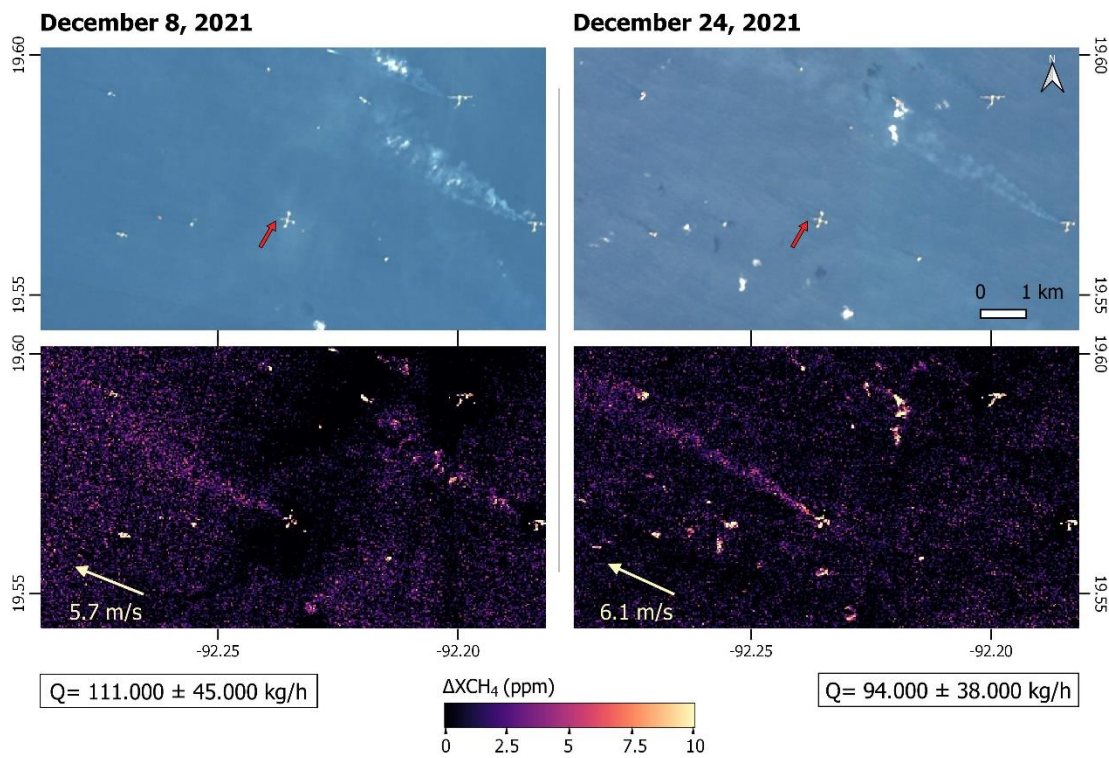

Figure S10: Results of the L8 images during the event. Above visual images (RGB) of the two days, and below the results of the CH4 retrieval in ppm corresponding to the same area.